Catal Lett (2008) 126:224–230
DOI 10.1007/s10562-008-9650-y

Electron Microscopy Study of γ-Al_2O_3 Supported Cobalt Fischer–Tropsch Synthesis Catalysts

Øyvind Borg · John C. Walmsley · Roya Dehghan · Bjørn S. Tanem · Edd A. Blekkan · Sigrid Eri · Erling Rytter · Anders Holmen

Received: 5 June 2008 / Accepted: 8 September 2008 / Published online: 2 October 2008

Abstract Three supported catalysts containing 20 wt% cobalt and 0.5 wt% rhenium were subjected to electron microscopy studies in their calcined state. The catalysts were prepared by incipient wetness impregnation of γ-Al_2O_3 supports of different pore characteristics with aqueous solutions of cobalt nitrate hexahydrate and perrhenic acid. The influence of the support on the Co_3O_4 crystallite size and distribution was studied by X-ray diffraction and electron microscopy. There was a positive correlation between the pore diameter of the support and the post calcination Co_3O_4 crystallite size. On all three γ-Al_2O_3 supports, Co_3O_4 was present as aggregates of many crystallites (20–270 nm in size). Cobalt oxide did not crystallise as independent crystallites, but as an interconnected network, with a roughly common crystallographic orientation, within the matrix pore structure. The internal variations in crystallite size between the catalysts were maintained after reduction. Fischer–Tropsch synthesis was carried out in a fixed-bed reactor at industrial conditions ($T = 483$ K, $P = 20$ bar, $H_2/CO = 2.1$). Although the cobalt-time yields varied significantly (4.6–6.7 $\times$ 10^{-3} mol CO/mol Co s), the site-time yields were constant (63–68 $\times$ 10^{-3} s^{-1}) for the three samples. The C_{5+} selectivity could not be correlated to the cobalt oxide aggregate size and is more likely related to the cobalt particle size and chemical properties of the γ-Al_2O_3 support.

Keywords Fischer–Tropsch synthesis · Cobalt · Rhenium · TEM · Pore diameter · Porosity

1 Introduction

Cobalt is favoured for the synthesis of long-chain hydrocarbons from natural gas-based synthesis gas because of its high activity, high selectivity to linear paraffins, high resistance towards deactivation, and low water-gas shift activity. In order to maximise the exposure of cobalt to gaseous reactants, it is normally dispersed on a high surface area support. Common supports include γ-Al_2O_3, SiO_2, and TiO_2. The choice of support is important for the final Fischer–Tropsch synthesis catalyst. However, site-time yields on supported cobalt catalysts are traditionally considered independent of support identity and cobalt dispersion [1–7]. Thus, the catalyst productivity can be predicted directly from the number of cobalt atoms deposited on the surface. Iglesia et al. [1–3] found constant site-time yield for the cobalt dispersion range 0.45–9.5%, which includes most of the typical low-dispersion cobalt Fischer–Tropsch catalysts. This cobalt dispersion range corresponds to a particle size range from 10 nm to 210 nm if cobalt oxide can be completely reduced to metal. However, for cobalt supported on carbon nanofibers, it has recently been shown that the site-time yield is lower for particles smaller than 8 nm in size [8].

Ø. Borg · E. A. Blekkan · E. Rytter · A. Holmen (✉)
Department of Chemical Engineering, Norwegian University of Science and Technology, 7491 Trondheim, Norway
e-mail: anders.holmen@chemeng.ntnu.no

Present Address:
Ø. Borg · S. Eri · E. Rytter
Statoil R&D, Research Centre, Postuttak, 7005 Trondheim, Norway

J. C. Walmsley · B. S. Tanem
SINTEF Materials and Chemistry, 7465 Trondheim, Norway

R. Dehghan
Department of Physics, Norwegian University of Science and Technology, 7491 Trondheim, Norway

While the influence of the support on Fischer–Tropsch activity is reasonably well-established, the impact on product selectivity is not equally clear. Many investigations [7, 9–12] have reported a strong influence of pore diameter on the C_{5+} selectivity. Iglesia et al. [1, 13, 14] proposed that the differences in selectivity observed for cobalt on different supports are due to variations in the extent of α-olefin re-adsorption. Neither the cobalt particle size, support, nor bimetallic effects are considered to influence the intrinsic chain growth probability on cobalt surfaces [1, 13, 14]. Shi and Davis [15], on the other hand, reported that diffusion limitations for the α-olefin products and their subsequent re-incorporation as chain initiators do not have a major impact on the product distribution. Bezemer et al. [8] recently reported a strong influence of the cobalt particle size on the performance in Fischer–Tropsch synthesis. At 35 bar, the C_{5+} selectivity decreased from 85% to 51% when the cobalt particle size was reduced from 16 nm to 3 nm. However, the C_{5+} selectivity was not calculated at the same CO conversion level for all five catalysts. A range in CO conversion between 13% and 84% provided the basis for the selectivity calculations. There is, however, a strong correlation between CO conversion and C_{5+} selectivity. Also, the experiments were conducted at two different temperatures.

To conclude, no unequivocal explanation seems to exist for the role of the support in the literature. However, like Bezemer et al. [8], we recently suggested that the particle size plays an important role for the product selectivity [10]. However, our study was silent about a possible impact of cobalt distribution. This paper, therefore, presents transmission electron microscopy images of selected catalysts from our recent investigation and relates these to the catalytic performance. Three catalysts that gave significant variations in C_{5+} selectivity were chosen. In order to reveal the microstructures as clearly as possible, samples were prepared for electron microscopy by ultramicrotomy [16].

2 Experimental

2.1 Catalyst Preparation

Three supported catalysts containing 20 wt% cobalt and 0.5 wt% rhenium were prepared by one-step incipient wetness co-impregnation of different Al_2O_3 supports (Sasol GmbH Puralox series) with aqueous solutions of cobalt nitrate hexahydrate and perrhenic acid. The supports (53–90 μm) were pre-calcined in flowing air at 773 K for 10 h prior to impregnation. A heating rate of 1 K/min was used to heat the samples from ambient temperature to 773 K.

All catalysts were dried at 393 K for 3 h after impregnation. Calcination at 573 K for 16 h in flowing air completed the preparation process. The temperature was increased by 2 K/min from ambient temperature to 573 K. Finally, the catalysts were sieved and the 53–90 μm fractions collected. Further treatment was done in situ.

The supports were named according to their pore sizes: "NPA" (narrow pore alumina), "MPA" (medium pore alumina), and "WPA" (wide pore alumina). After cobalt and rhenium impregnation, the catalyst nomenclature was "CoRe/NPA", "CoRe/MPA", and "CoRe/WPA".

The Fischer–Tropsch synthesis activity and selectivity of these catalysts have been presented previously [10].

2.2 Support and Catalyst Characterisation

2.2.1 Nitrogen Adsorption/Desorption

Nitrogen adsorption–desorption isotherms were measured on a Micromeritics TriStar 3000 instrument at liquid nitrogen temperature, 77 K. The samples (0.3 g, 53–90 μm) were outgassed at 573 K overnight prior to measurement.

The surface area was calculated from the Brunauer–Emmett–Teller (BET) equation [17], while the total pore volume and pore size distribution were found applying the Barrett–Joyner–Halenda (BJH) method [18]. The nitrogen desorption branch was chosen for pore size analysis.

2.2.2 X-ray Diffraction

X-ray diffraction patterns were recorded for all the supports and catalysts at ambient temperature on a Siemens D5005 X-ray diffractometer using Cu$K\alpha$ radiation. The samples were crushed prior to measurement. The scans were recorded in the 2θ range between 10 and 90° using a step size of 0.04°. Peaks were identified by comparison with standards in a database.

The average cobalt oxide crystallite thickness was calculated from the Scherrer equation [19] using the (311) Co_3O_4 peak located at $2\theta = 36.9°$. A K factor of 0.89 was used in the Scherrer formula [19]. Lanthanum hexaboride was used as reference material to determine the instrumental line broadening.

2.2.3 Hydrogen Chemisorption

Hydrogen adsorption isotherms were recorded on a Micromeritics ASAP 2010C unit. The samples (0.5 g, 53–90 μm) were evacuated at 313 K for 1 h, and then reduced in situ in flowing hydrogen at 623 K for 16 h. The temperature was increased by 1 K/min from 313 to 623 K. After reduction, the samples were evacuated for 1 h at 603 K, and for 30 min at 373 K before cooling to 313 K. The adsorption isotherm was recorded in the pressure interval ranging from 20 to 510 mmHg. The amount of

chemisorbed hydrogen was determined by extrapolating the straight-line portion of the isotherm to zero pressure. Furthermore, in order to calculate the dispersion, it was assumed that two cobalt surface atoms were covered by one hydrogen molecule [20], and that rhenium did not contribute to the amount of hydrogen adsorbed.

The apparent cobalt metal particle size ($d(Co^0)_{uncorrected}$) can be calculated from the cobalt dispersion (D) by assuming spherical, uniform cobalt metal particles with site density of 14.6 at./nm^2 [21]. These assumptions give the following formula:

$$d\left(Co^0\right)_{uncorrected}(nm) = \frac{96}{D(\%)} \quad (1)$$

Since the reducibility of metal oxide supported cobalt catalysts can be low, it is necessary to correct Eq. 1 for the degree of reduction (DOR). Thus, the corrected cobalt particle size is:

$$d\left(Co^0\right)_{corrected}(nm) = \frac{96}{D(\%)} \cdot DOR. \quad (2)$$

2.2.4 Electron Microscopy

For ultramicrotomy TEM sample preparation, small amounts of the catalysts were embedded in a two component epoxy resin and stored overnight at room temperature. Thin slices (nominally $\sim$50 nm) were obtained by cutting the embedded catalyst with a diamond knife using a Reichert-Jung ultramicrotome and collected on a standard perforated carbon support Cu mesh grid. TEM analysis was performed using a JEOL 2010F instrument operating at 200 kV equipped with an Oxford Instruments X-ray detector for energy dispersive spectroscopy (EDS) composition analysis. Conventional TEM was performed under bright-field diffraction contrast conditions. For EDS, the microscope was operated in scanning transmission electron microscopy (STEM) mode with a nominal probe diameter of $\sim$0.7 nm. STEM images were acquired using an annular dark field detector which provides contrast that has a strong dependence on atomic number. This is particularly useful for distinguishing higher atomic number catalyst particles, which appear relatively bright, from a lower atomic number support.

2.3 Fischer–Tropsch Synthesis

Fischer–Tropsch synthesis was performed in a fixed-bed reactor (stainless steel, 10 mm inner diameter). The samples (1.0 g, 53–90 μm) were diluted with inert silicon carbide particles (20.0 g, 75–150 μm) in order to improve the temperature distribution along the catalytic zone.

The samples were reduced in situ in hydrogen at 1 bar while the temperature was increased at 1 K/min to 623 K. After 16 h of reduction, the catalysts were cooled to 443 K. The system was then pressurised to 20 bar and synthesis gas of molar ratio $H_2/CO = 2.0$ (and 3% N_2 as internal standard) was introduced to the reactor. To avoid run-away and catalyst deactivation at start-up, the temperature was increased slowly to the reaction temperature 483 K.

Each experiment was divided into two periods which lasted for 24 and 76 h, respectively. The following conditions were used:

Period 1: Synthesis gas at a flow rate of 250 N mL/min.
Period 2: Synthesis gas at an adjusted flow rate to give a target CO conversion of 50%.

Heavy hydrocarbons were collected in a heated trap (363 K) and liquid products were removed in a cold trap (298 K). The effluent gaseous product was analysed for hydrogen, nitrogen, carbon monoxide, carbon dioxide, water, and C_1 to C_9 hydrocarbons using an on-line Agilent 6890 gas chromatograph equipped with a thermal conductivity detector and a flame ionisation detector.

Activity is reported as cobalt-time yield (mol CO/(mol Co s)). The C_{5+} selectivity was calculated by subtracting the amount of C_1–C_4 hydrocarbons and CO_2 in the product gas mixture from the total mass balance.

3 Results and Discussion

3.1 Support and Catalyst Characterisation

3.1.1 N_2 Adsorption/Desorption

Nitrogen adsorption/desorption isotherms showed that three types of hysteresis loops and, therefore, three types of pore geometries were represented by the three supports. In the absence of a universal model, the Barrett–Joyner–Halenda model was chosen for calculation of pore sizes. Figure 1 gives the pore size distributions of the γ-Al_2O_3 supports and the corresponding impregnated samples. Although the starting support in all cases was γ-Al_2O_3, the physical parameters varied significantly. Impregnation, drying, and calcination did not significantly modify the pore size distributions, but reduced the nitrogen uptake. Table 1 gives surface areas and pore size data.

3.1.2 X-ray Diffraction

X-ray diffraction patterns of all the calcined catalysts confirmed the presence of crystalline phases γ-Al_2O_3 and Co_3O_4 [10]. However, the line width of the Co_3O_4 peaks was different for the various catalysts. Thus, the Co_3O_4 crystallite size varied. The third column of Table 1 and the second column of Table 2 indicate that the Co_3O_4

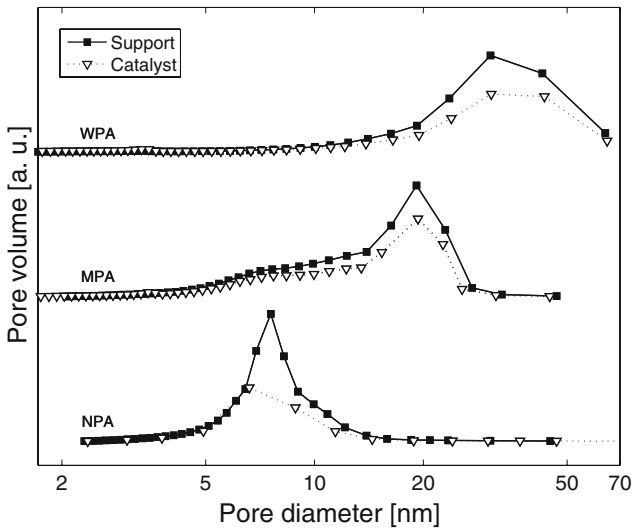

Fig. 1 Support and catalyst pore size distributions calculated from the nitrogen desorption branches using the Barrett–Joyner–Halenda method (filled symbol = support, open symbol = catalyst)

Table 1 Nitrogen adsorption/desorption data

Sample	BET surface area (m^2/g)	Average pore diameter (nm)	Pore volume (cm^3/g)	Porosity
NPA	184	7.4	0.48	0.66
CoRe/NPA	143	7.1	0.30	0.55
MPA	191	11.6	0.78	0.76
CoRe/MPA	149	11.6	0.51	0.67
WPA	114	26.7	0.96	0.78
CoRe/WPA	92	23.7	0.57	0.69

The experimental error ($\pm 2\sigma$) is ± 5 m^2/g for the surface areas, ± 0.2 nm for the average pore diameters and ± 0.02 cm^3/g for the pore volumes. The uncertainty is based on three independent runs of all the samples

crystallite size could be correlated with the support pore diameter. Largest Co_3O_4 crystallites were found in the support of widest pores. The same relationship has previously been demonstrated for a series of 10 other γ-Al_2O_3 supported cobalt catalysts [10]. Table 2 also shows that the corrected cobalt metal particle size after catalyst activation was related to the post calcination Co_3O_4 crystallite size.

For two of the catalysts (CoRe/NPA and CoRe/MPA), the average Co_3O_4 crystallite size was larger than the calculated average support pore diameter. Thus, the majority of the crystallites were apparently located on the exterior of these supports. However, comparison of pore diameter and Co_3O_4 crystallite size for location of the crystallites should be done with care. In fact, we believe that the crystallites were located inside the pore system and relate the conflicting results to the choice of pore geometry model. The Barrett–Joyner–Halenda model assumes presence of only cylindrical pores and absence of pore networks. In reality, no simple pore geometry exists as demonstrated by Rytter et al. [22]. Transmission electron microscopy images of the Co/γ-Al_2O_3 interphase showed that the alumina crystallites were entangled into each other in what appeared to be a chaotic fashion. The cobalt aggregates stretched over a number of alumina crystallites and so-called pores. To conclude, the calculated Co_3O_4 crystallite size can very well be larger than the calculated pore size even though the crystallites actually are located inside the pores.

3.1.3 *Electron Microscopy*

Before continuing, it is important to bear in mind that the electron microscopy observations were made on the cubic Co_3O_4 phase, after impregnation, drying, and calcination, but before reduction. During reduction, the cubic oxide phase will transform to the hexagonal metallic phase. Some fine-scale changes in the catalyst particle morphology are to be expected during the reduction process. Nevertheless, Fig. 2 shows a dark-field STEM micrograph and complementary mapping of catalyst CoRe/MPA. In Fig. 2a, Co_3O_4 appears as bright, spherical aggregates embedded in the surrounding amorphous γ-Al_2O_3 support. The support appears grey relative to the Co_3O_4 because of its lower relative atomic number. The distribution of the phases shown in the STEM image was confirmed by EDS mapping of Co, Re, Al and O in the same field of view (Fig. 2b–e). The Re EDS signal has a very poor signal-to-noise ratio because of the low concentration (0.5 wt%). As the EDS

Table 2 Cobalt particle size data

Catalyst	Co_3O_4 crystallite size (nm)	Dispersion (%)	$d(Co^0)_{uncorrected}$[a] (nm)	Degree of reduction (%)	$d(Co^0)_{corrected}$[b] (nm)
CoRe/NPA	12.0	8.7	11.1	63	6.9
CoRe/MPA	14.6	7.9	12.2	74	9.1
CoRe/WPA	21.1	6.5	14.9	76	11.4

The experimental error ($\pm 2\sigma$) is less than ± 1 nm for the Co_3O_4 crystallite sizes calculated from X-ray diffraction and less than ± 0.5 nm for the cobalt metal particle sizes calculated from hydrogen chemisorption data. The uncertainty is based on three independent runs of all the catalysts

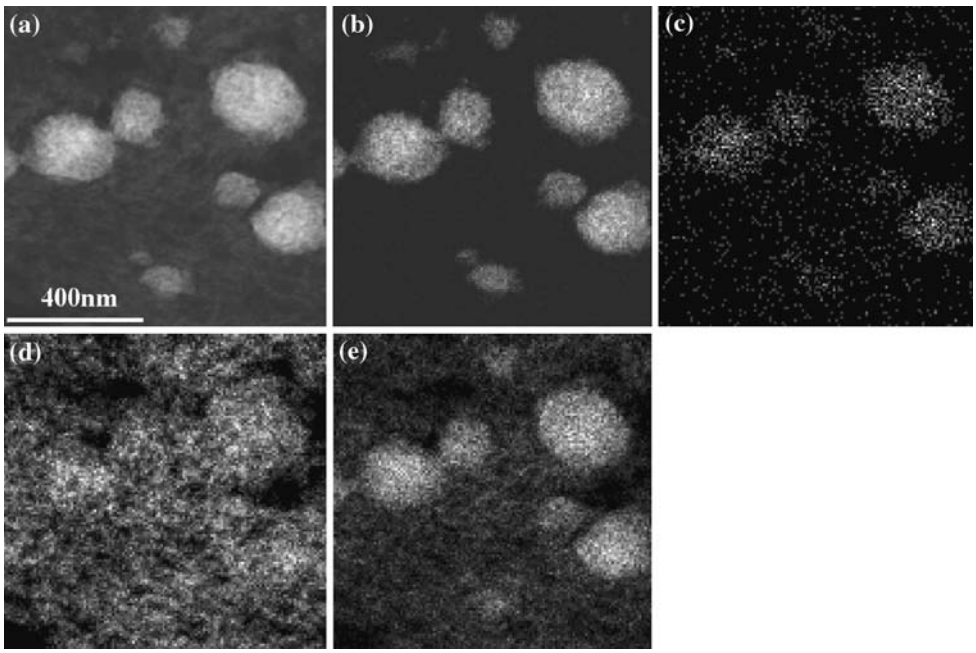

Fig. 2 Dark-field STEM micrograph and complementary composition mapping of catalyst CoRe/MPA. (**a**) STEM image. (**b**) Co EDS map. (**c**) Re EDS map. (**d**) Al EDS map. (**e**) O EDS map

background signal increased in the region of Co_3O_4 aggregates, the Re map alone is not reliable evidence of the localisation of this element. However, EDS spectra extracted from the mapping data at the positions of the Co_3O_4 aggregates showed weak, but clear, characteristic Re peaks. Similar spectra extracted from the area of the γ-Al_2O_3 support showed no Re peaks, indicating that most or all of the Re was associated with the Co_3O_4.

Bright-field TEM micrographs of catalyst CoRe/MPA is shown in Fig. 3. Due to the higher density and stronger diffraction from the more crystalline Co_3O_4 crystallites relative to the γ-Al_2O_3 support, the Co_3O_4 aggregates are black and the alumina support grey. Lower magnification images included a sufficient number of aggregates to allow measurement of a reliable average aggregate size. The aggregate diameter measurements were corrected for underestimation of the true value due to cutting of the aggregates at the bottom and top surfaces of the sample. Diameters of around 100 aggregates from each sample were measured and divided into bins of 5 nm. A correction was then calculated to correct for the finite thickness of the sample [23]. The latter was taken to be 50 nm, the nominal thickness for the microtomed slices studied, although this was not measured exactly. As shown in Table 3, there were some differences in the average Co_3O_4 aggregate sizes between the three materials. While the average aggregate size of CoRe/NPA was 83 nm, the corresponding sizes of catalysts CoRe/MPA and CoRe/WPA were similar and close to 120 nm.

More detailed analysis of the Co_3O_4 aggregates shows that these can tend to grow with crystallites roughly aligned in a common crystallographic orientation. This is

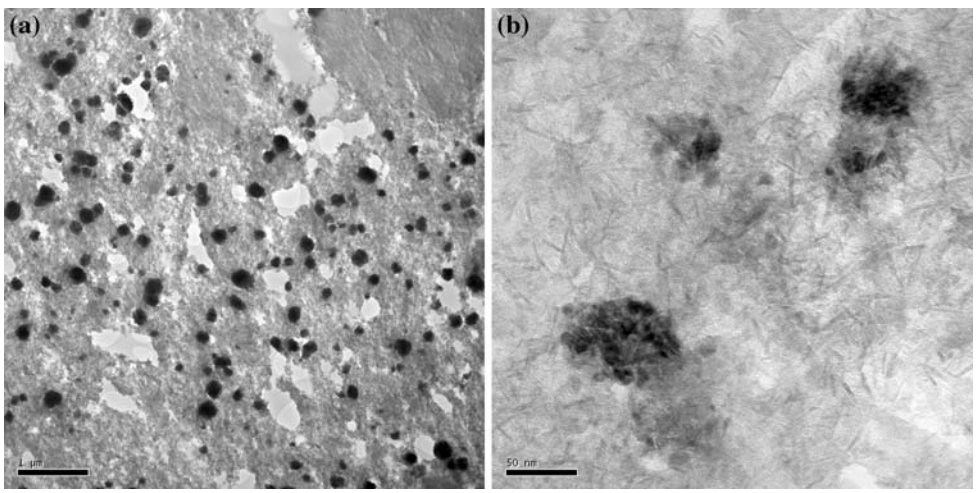

Fig. 3 Bright-field TEM micrographs of catalyst CoRe/MPA (sample at low magnification (**a**), structure of the support and cobalt aggregates in finer detail (**b**))

Table 3 Corrected average Co_3O_4 aggregate size

Sample	Aggregates between (nm)	Corrected average aggregate size (nm)	Numbers of aggregates measured
CoRe/NPA	20–230	87	100
CoRe/MPA	30–270	134	185
CoRe/WPA	30–250	113	175

The uncertainty in the average aggregate size is approximately ±15 nm

illustrated in Fig. 4 which shows bright-field (a), and dark-field (b), images of a single cluster and the diffraction pattern obtained from it (c). The dark-field image shows bright contrast over the whole cluster, suggesting a common diffraction condition for most of the crystallites in the aggregate. This is confirmed by the diffraction pattern that was recorded from an area in the sample including the entire aggregate. It shows a quite clean systematic row based on the (220) Co_3O_4 reflection. Other details in the diffraction pattern are due to discrete, randomly oriented, Co_3O_4 crystallites in the aggregate and the alumina support. Arslan et al. [24] have recently used electron tomography to show the detailed three dimensional morphology of a Co_3O_4 aggregate in a similar γ-alumina supported catalyst. The Co_3O_4 and support were found to form a dense interlocking network, with the former filling the pores of the latter. The electron tomography results were not sensitive to crystallographic orientation and the observation in Fig. 4 is complementary showing an overall crystallographic alignments of the crystallites within the aggregate. Since cobalt crystallised as an interconnected network, the aggregate size (Table 3) was lower for the catalyst with lowest porosity (Table 1), CoRe/NPA, than catalysts CoRe/MPA and CoRe/WPA. Storsæter et al. [16] also attributed the larger aggregates present on SiO_2 than on γ-Al_2O_3 to the higher porosity of the SiO_2 support. Feller et al. [25] related the size of the clusters to the size of the cobalt nitrate droplet during the drying process.

3.2 Fischer–Tropsch Synthesis

Cobalt and site-time yields recorded after 8 h on stream are given in Table 4. Although the cobalt-time yields varied (4.6–6.7 $\times$ 10^{-3} mol CO/mol Co s), the site-time yields were constant (58–64 $\times$ 10^{-3} s^{-1}). It should be mentioned that Bezemer et al. [8] found cobalt particles smaller than 8 nm in size to be less active than larger particles. No such difference was found in this investigation. However, note that only one catalyst had an average particle size below 8 nm in size (CoRe/NPA) and that the calculated particle size is dependent on the H_2 chemisorption and O_2 pulse titration measurement conditions. Also, the cobalt particle size distribution is unknown. Thus, there is not sufficient data to draw any conclusions about a possible particle size effect on the cobalt intrinsic activity.

Significant variations in C_{5+} selectivity were observed. At constant CO conversion level, the numbers were 81.7, 83.4, and 84.9% for catalysts CoRe/NPA, CoRe/MPA, and CoRe/WPA. These numbers can be positively correlated to both the pore diameter and the particle size. However, we [10] indicated in our previous investigation that the pore diameter most likely plays a minor role for the selectivity. This was later confirmed by Rytter et al. [22]. In the

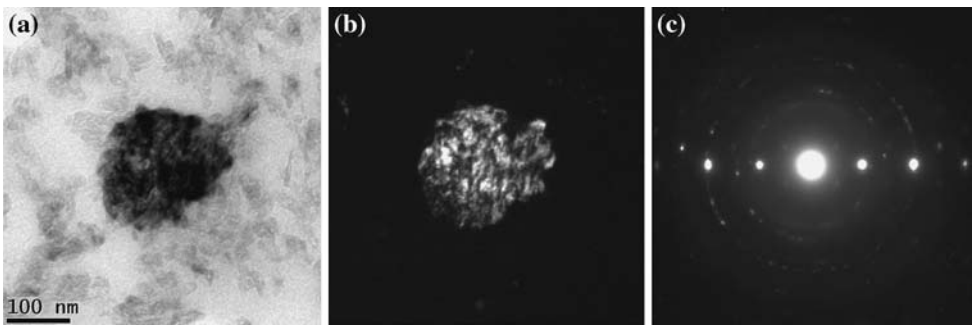

Fig. 4 Bright-field and dark-field image and a diffraction pattern recorded from an aggregate in catalyst CoRe/MPA

Table 4 Cobalt-time yields and site-time yields calculated after 8 h on stream (T = 483 K, P = 20 bar, H_2/CO = 2.1 and GHSV = 15 Nl/(g_{cat} h)) and C_{5+} selectivity recorded at 43–44% CO conversion

Catalyst	Initial cobalt-time yield $\times$ 10^3 (mol CO/(mol Co s))	Initial site-time yield $\times$ 10^3 (s^{-1})	C_{5+} selectivity (%)
CoRe/NPA	6.7	63	81.7
CoRe/MPA	6.2	64	83.4
CoRe/WPA	4.6	58	84.9

The experimental error ($\pm 2\sigma$) is $\pm 5 \times 10^{-3}$ s^{-1} and ±0.5% for the site-time yield and C_{5+} selectivity, respectively

present work, there was an apparent close correlation between the selectivity level and the cobalt particle size in the range 7–11 nm. Bezemer et al. [8] also found the particle size to impact the C_{5+} selectivity, but only for particles between 3 nm and 8 nm in size. Although the data of the present investigation indicate that their results can be extended to larger particles, we also believe that the chemical properties of the γ-Al_2O_3 support are important for the variations in selectivity. Furthermore, there are no indications that the Co_3O_4 cobalt distribution (e.g. aggregate size) plays an important role for the C_{5+} selectivity level as evident from Tables 3 and 4. Nevertheless, it should be mentioned that Storsæter et al. [16] observed that when Co_3O_4 appeared as single crystallites on α-Al_2O_3 and TiO_2, the C_{5+} selectivity was high. For γ-Al_2O_3, Co_3O_4 was located in aggregates and the selectivity to long-chain hydrocarbons was lower.

4 Conclusions

Catalyst particle size and distribution was studied in three γ-Al_2O_3 supported cobalt catalysts having different pore characteristics. X-ray diffraction showed that the dominant cobalt phase after calcination was Co_3O_4. Electron microscopy images showed that Co_3O_4 appeared in aggregates, intergrown through the support pore structure, of many individual Co_3O_4 crystallites. The size of the aggregates was found to correlate with the porosity of the samples. X-ray diffraction crystallite size data indicated a positive correlation between the Co_3O_4 crystallite size and the average pore diameter of the support. The starting support had a great impact on the final Fischer–Tropsch catalyst and performance. Further work is required to characterise the microstructural features obtained by TEM and to more accurately correlate these with the catalyst performance.

Acknowledgments The financial support from the Research Council of Norway and Statoil is greatly acknowledged.

References

1. Iglesia E, Soled SL, Fiato RA (1992) J Catal 137:212
2. Iglesia E (1997) Appl Catal A 161:59
3. Iglesia E (1997) Stud Surf Sci Catal 107:153
4. Oukaci R, Singleton AH, Goodwin JG Jr (1999) Appl Catal A 186:129
5. Bertole CJ, Mims CA, Kiss G, Joshi P (2001) Stud Surf Sci Catal 136:369
6. Bertole CJ, Mims CA, Kiss G (2004) J Catal 221:191
7. Storsæter S, Borg Ø, Blekkan EA, Holmen A (2005) J Catal 231:405
8. Bezemer GL, Bitter JH, Kuipers HPCE, Oosterbeek H, Holewijn JE, Xu X, Kapteijn F, van Dillen AJ, de Jong KP (2006) J Am Chem Soc 128:3956
9. Saib AM, Claeys M, van Steen E (2002) Catal Today 71:395
10. Borg Ø, Eri S, Blekkan EA, Storsæter S, Wigum H, Rytter E, Holmen A (2007) J Catal 248:89
11. Xiong H, Zhang Y, Wang S, Li J (2005) Catal Commun 6:512
12. Song D, Li J (2006) J Mol Catal A 247:206
13. Iglesia E, Soled SL, Fiato RA, Via GH (1993) J Catal 143:345
14. Iglesia E, Soled SL, Fiato RA, Via GH (1994) Stud Surf Sci Catal 81:433
15. Shi B, Davis BH (2005) Catal Today 106:129
16. Storsæter S, Tøtdal B, Walmsley JC, Tanem BS, Holmen A (2005) J Catal 236:139
17. Brunauer S, Emmett PH, Teller E (1938) J Am Chem Soc 60:309
18. Barrett EP, Joyner LG, Halenda PP (1951) J Am Chem Soc 73:373
19. Scherrer P (1918) Göttingen Nachrichten 2:98
20. Reuel RC, Bartholomew CH (1984) J Catal 85:63
21. Jones RD, Bartholomew CH (1988) Appl Catal 39:77
22. Rytter E, Eri S, Skagseth TH, Schanke D, Bergene E, Myrstad R, Lindvåg A (2007) Ind Eng Chem Res 46:9032
23. Andersen SJ, Holme B, Marioara CD (2008) Ultramicroscopy 108:750
24. Arslan I, Walmsley JC, Rytter E, Bergene E, Midgley PA (2008) J Am Chem Soc 130:5716
25. Feller A, Claeys M, van Steen E (1999) J Catal 185:120